npj | quantum information

Article

Published in partnership with The University of New South Wales

https://doi.org/10.1038/s41534-025-01151-5

True decoherence-free-subspace derived from a semiconductor double quantum dot Heisenberg spin-trimer

Wonjin Jang[1,2], Jehyun Kim[1,3], Jaemin Park[1], Min-Kyun Cho[1,4], Hyeongyu Jang[1], Sangwoo Sim[1], Hwanchul Jung[5], Vladimir Umansky[3] & Dohun Kim[1]

Spins in solid systems can inherently serve as qubits for quantum simulation or quantum information processing. Spin qubits are usually prone to environmental magnetic field fluctuations; however, a spin qubit encoded in a decoherence-free-subspace (DFS) can be protected from certain degrees of environmental noise depending on the specific structure of the DFS. Here, we derive the "true" DFS from an antiferromagnetic Heisenberg spin-1/2 trimer, which protects the qubit states against both short- and long-wavelength magnetic field fluctuations. We define the spin trimer with three electrons confined in a gate-defined GaAs double quantum dot (DQD) where we exploit Wigner-molecularization in one of the quantum dots. We first utilize the trimer for dynamic nuclear polarization (DNP), which generates a sizable magnetic field difference, ΔB_z, within the DQD. We show that large ΔB_z significantly alters the eigenspectrum of the trimer and results in the "true" DFS in the DQD. Real-time Bayesian estimation of the DFS energy gap explicitly demonstrates protection of the DFS against short-wavelength magnetic field fluctuations in addition to long-wavelength ones. Our findings pave the way toward compact DFS structures for exchange-coupled quantum dot spin chains, the internal structure of which can be coherently controlled completely decoupled from environmental magnetic fields.

The semiconductor quantum dot (QD) system represents a platform for the exploration of interacting electrons where the electrons confined in QDs are often described by the Fermi-Hubbard model[1,2]. In particular, when direct charge transitions between adjacent QDs are forbidden, in analogy to the Mott-insulating phase[3], QDs can still exchange their spins via exchange interactions[4,5]. These systems allow quantum simulations[6–8] and magnetic-field-free encoding of spin qubits[9,10], and can thus be considered a scalable resource for practical quantum computations.

While the environment coupled to a qubit can lead to undesired decoherence, qubit states encoded in a decoherence-free-subspace (DFS) can be protected against certain fluctuations in the environment[11,12]. Several types of QD qubit encoding in DFS have been proposed considering protection from electric and long- and short-wavelength magnetic noise compared with the system size[13]. Examples include charge quadruple DFS to overcome dipolar charge noise[14] or singlet-triplet qubits to protect against long-wavelength magnetic field fluctuations[4,15]. Recently, more elaborate schemes such as singlet-only encoding in a triple QD (TQD)[16] have been theoretically shown to form a "true" DFS, which screens both short- and long-wavelength fluctuations. However, explicit demonstrations of such yet remain elusive, where a simpler structure may facilitate experimental realization of the "true" DFS.

The derivation of a DFS requires tunable energy levels which are accessible within the experimental bandwidth[14,16,17], where Coulomb correlation effects may provide controllable low-lying energy states for such applications[18,19]. Initially proposed as a few-electron counterpart of a Wigner crystal[20], Coulomb correlation-driven Wigner molecularization in QDs[18,19,21,22] has been drawing much attention for its relevance to quantum information science[19,23,24]. Along with ground state localization[25], the Wigner molecularization further quenches the orbital splitting from 10^2 μeV to the microwave-accessible 10^0 μeV regime, as demonstrated in

[1]NextQuantum, Department of Physics and Astronomy, and Institute of Applied Physics, Seoul National University, Seoul, South Korea. [2]Institute of Physics and Center for Quantum Science and Engineering, École polytechnique fédérale de Lausanne (EPFL), Lausanne, Switzerland. [3]Braun Center for Submicron Research, Department of Condensed Matter Physics, Weizmann Institute of Science, Rehovot, Israel. [4]Center for Superconducting Quantum Computing System, Korea Research Institute of Standards and Science, Daejeon, South Korea. [5]Department of Physics, Pusan National University, Busan, South Korea.
e-mail: dohunkim@snu.ac.kr

carbon-nanotube[26], Si[27], GaAs[23,24] and Ge[28] QDs. In addition to spin qubit operations exploiting the reduced energy gap of the Wigner molecule (WM) states[23], engineering of the states may further promote coherent DFS structures, which stays unexplored to date.

In this work, we derive a "true" DFS robust to both short- and long-wavelength magnetic fluctuation from an exchange-coupled spin-1/2 trimer. We define the trimer with three electrons confined in a gate-defined GaAs double QD (DQD), where the Wigner-molecularization in one of the QDs quenches the excitation spectrum of the trimer down to <2 GHz·h (h is Planck's constant). Exploiting the dynamic nuclear polarization (DNP) enabled by the Wigner-molecularization[24], we build the spatial magnetic field difference, ΔB_z, between the two QDs. A large ΔB_z is shown to significantly alter the eigenstates of the trimer and result in a "true" DFS in the DQD, in contrast to previously proposed schemes requiring a TQD[16] or a quadruple QD array[17]. Real-time Bayesian Hamiltonian estimation[29–31] confirms that the fluctuation of the energy gap between DFS states is smaller than that of the states outside the DFS, proposing a magnetic-noise-resilient spin qubit based on exchange interactions in a DQD.

Results

True decoherence-free-subspace in a Heisenberg spin-1/2 trimer

We first elucidate the "true" DFS which can be found in a Heisenberg spin-1/2 trimer. Figure 1a illustrates three spin-1/2 particles interacting with each other by antiferromagnetic exchange interaction. Here, $\mathbf{S}_i$ denotes the spin state of the i^{th} particle and J_{ij} represents the exchange interaction between $\mathbf{S}_i$ and $\mathbf{S}_j$. We assume a trimer where $\mathbf{S}_1$ and $\mathbf{S}_2$ are placed close to each other in the site on the left, and $\mathbf{S}_3$ is placed in the site on the right, separated by d_{LR} from that on the left. This results in $J_{12} \gg J_{LR} = (J_{23} + J_{31})/2$, where J_{12} (J_{LR}) presents intra (inter) site exchange interaction. Taking into account the magnetic field difference $\Delta B_z = B_z^L - B_z^R$ between the sites, the Hamiltonian of the system is described below (Eqn. 1). Here, $B_z^L = (B_{z,1} + B_{z,2})/2$ and $B_z^R = B_{z,3}$ are the average magnetic field strength along the z-axis in the left and right site respectively, where $B_{z,i}$ corresponds to the z-axis magnetic field strength experienced by the spin $\mathbf{S}_i$. We assume that the magnetic field difference between $\mathbf{S}_1$ and $\mathbf{S}_2$, $\delta b_{z,L} = (B_{z,1} - B_{z,2})$ is negligible. We consistently use a unit with $g^*\mu_B = 1$ to normalize the magnetic field to the energy (g^* is the gyro-magnetic ratio of the spin, and μ_B is the Bohr magneton.).

$$H = J_{12}\mathbf{S_1}\cdot\mathbf{S_2} + J_{23}\mathbf{S_2}\cdot\mathbf{S_3} + J_{31}\mathbf{S_3}\cdot\mathbf{S_1} + \Delta B_z/2\,(\mathbf{S}_1^z + \mathbf{S}_2^z - -\mathbf{S}_3^z) \quad (1)$$

At $\Delta B_z = 0$, the Hamiltonian results in doublet and quadruplet (Q) eigenstates with the total spin quantum number $S_{tot} = 1/2$ and 3/2, respectively[9,24]. Depending on the symmetry of the spin states, a doublet state can form either a doublet-singlet (D_S) or a doublet-triplet (D_T). In our case with $J_{12} \gg J_{LR}$, J_{12} dominates the D_S-D_T energy gap (inset to Fig. 1a)

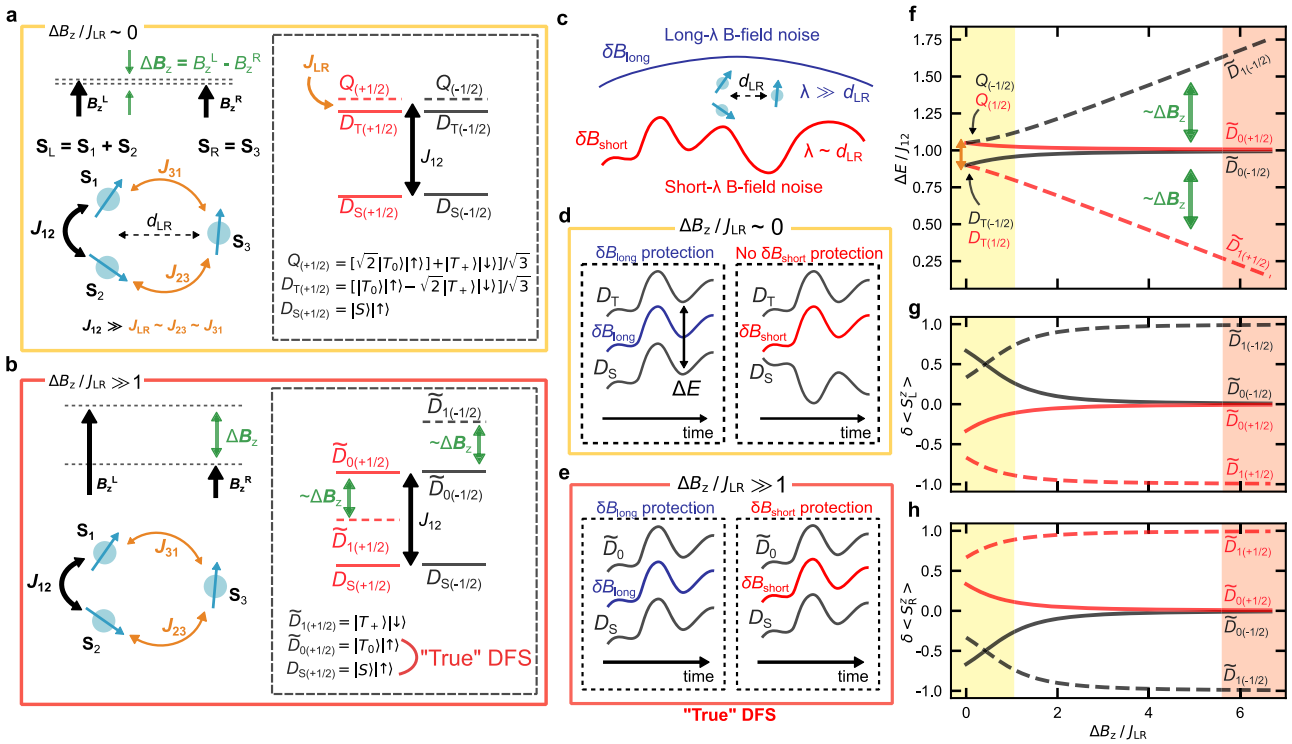

Fig. 1 | Eigenspectrum of a Heisenberg spin-trimer under magnetic field gradient. a Antiferromagnetic Heisenberg spin-1/2 trimer under a small magnetic field gradient. $\mathbf{S}_1$, $\mathbf{S}_2$, and $\mathbf{S}_3$ denote the spin states forming the trimer, where J_{ij} is the antiferromagnetic exchange interaction between $\mathbf{S}_i$ and $\mathbf{S}_j$. $\mathbf{S}_1$ and $\mathbf{S}_2$ are placed in close proximity in the site on the left, whereas $\mathbf{S}_3$ is placed in the site on the right relatively far away from $\mathbf{S}_1$ and $\mathbf{S}_2$, resulting in $J_{12} \gg J_{LR} = (J_{23} + J_{31})/2$ with J_{LR} being the inter-site exchange interaction. B_z^L (B_z^R) represents the magnetic field along the z-axis in the left (right) site. Inset (black dashed box): Eigenstates of the described trimer in $m_s = +1/2$ (red) and $m_s = -1/2$ (black) subspace under small magnetic field gradient $\Delta B_z = B_z^L - B_z^R$. D_S and D_T states define a qubit in each m_s subspace. The $|m_s| = 3/2$ states are omitted for simplicity (see Methods for explicit expression of the spin states). **b** Antiferromagnetic Heisenberg spin-1/2 trimer under large magnetic field gradient. Inset (black dashed box): Eigenstates of $m_s = +1/2$ (red) and $m_s = -1/2$ (black) subspace altered by large $\Delta B_z >> J_{LR}$ (see text for the unit). D_S and $\widetilde{D}_0$ states form a "true" decoherence-free-subspace robust to both long- and short-wavelength magnetic field noise. **c** Schematic of long- (short-) wavelength magnetic field noise δB_{long} (δB_{short}) shown as a blue (red) curve. The characteristic length scale of δB_{long} (δB_{short}) is longer than (comparable to) the physical scale of the trimer, d_{LR}. **d**, **e** Schematic of $D_{T(\pm1/2)}$–$D_{S(\pm1/2)}$ ($\widetilde{D}_{0(\pm1/2)}$–$D_{S(\pm1/2)}$) energy gap fluctuation along δB_{long} and δB_{short} in time. **f** Excitation energy spectrum of the Heisenberg spin trimer as a function of $\Delta B_z/J_{LR}$. Each curve illustrates the energy gap between the denoted state and the corresponding ground state $D_{S(+1/2)}$ or $D_{S(-1/2)}$. For the calculation $J_{LR} = 0.1J_{12}$ and $\delta J_{LR} = J_{31} - J_{23} = 0.05J_{12}$ is assumed. The energy splitting between D_T and Q states (orange arrow at $\Delta B_z/J_{LR} = 0$) is proportional to the size of J_{LR}. **g**, **h** Susceptibility to local magnetic field fluctuation in the left (right) site, as a function of $\Delta B_z/J_{LR}$. The difference in average z-axis spin value in the left (right) site, between the denoted state and the corresponding ground state, is evaluated (see text for details).

where D_S (D_T) involves the singlet (triplet) pairing of $\mathbf{S}_1$ and $\mathbf{S}_2$ in the left site (see Methods for explicit spin expressions). We note that the D_T-Q energy gap corresponds to $1.5J_{LR}$ (see Supplementary Note S1). The finite magnetic field splits each doublet (quadruplet) state into $m_s = +1/2$ and $-1/2$ ($+3/2$, $+1/2$, $-1/2$ and $-3/2$) states, where m_s represents the spin projection to the z-axis. We introduce a notation $A_{(ms)}$ to denote the spin state A and the corresponding m_s simultaneously. Importantly, $D_{S(\pm1/2)}$–$D_{T(\pm1/2)}$ form an encoded spin qubit controllable by exchange interactions[9,23,32]. Due to the spin selection rule, the exchange interaction only couples the states with the same S_{tot} and m_s[9], thereby facilitating effective qubit operations. Explicitly, in the ordered qubit basis [$D_{S(\pm1/2)}$, $D_{T(\pm1/2)}$] the spin-trimer Hamiltonian (Eqn. 1) reduces to H_{qubit} in Eq. 2 (see Supplementary Note S1 for the Hamiltonian represented in the full spin-trimer basis), where $\delta j_{LR}=J_{31}-J_{23}$ represents the difference in inter-site exchange interaction. Apparently, δj_{LR} is necessary to drive transition between the qubit states.

$$H_{\text{qubit}} = \begin{bmatrix} -\frac{3}{4}J_{12} & \frac{\sqrt{3}}{4}\delta j_{\text{LR}} \\ \frac{\sqrt{3}}{4}\delta j_{\text{LR}} & \frac{2}{3}\Delta B_z + \frac{1}{4}J_{12} - J_{\text{LR}} \end{bmatrix} \quad (2)$$

As is clear from Eq. 2, the eigenspectrum of the Heisenberg trimer is altered by finite ΔB_z, which also hybridizes $D_{T(\pm1/2)}$ and $Q_{(\pm1/2)}$ states (see Supplementary Note S1). Thereby, in the $|\Delta B_z| < J_{LR}$ regime, ΔB_z modulates the $D_{S(\pm1/2)}$–$D_{T(\pm1/2)}$ energy gap $\Delta E(D_{T(\pm1/2)}) = E(D_{T(\pm1/2)})$–$E(D_{S(\pm1/2)})$. Here, $E(A_{(ms)})$ denotes the energy of $A_{(ms)}$. However, when $|\Delta B_z| \gg J_{LR}$, ΔB_z significantly transforms the eigenspectrum. For example, in the $m_s = +1/2$ subspace under $|\Delta B_z| \gg J_{LR}$, $\widetilde{D}_{0(+1/2)} = |T_0\rangle|\uparrow\rangle$ and $\widetilde{D}_{1(+1/2)} = |T_+\rangle|\downarrow\rangle$, whose energies are separated by ΔB_z, become the eigenstates of Eqn. 1 (inset to Fig. 1b) instead of $D_{T(+1/2)}$ and $Q_{(+1/2)}$ for ΔB_z=0. Due to the hybridization, both $\widetilde{D}_{0(\pm1/2)}$ and $\widetilde{D}_{1(\pm1/2)}$ are exchange-coupled to $D_{S(\pm1/2)}$, where the energy separation given by ΔB_z allows selective addressing of each state (inset to Fig. 1b). As detailed below, $\widetilde{D}_{0(\pm1/2)}$ and $D_{S(\pm1/2)}$ form a "true" DFS decoupled from both short- and long-wavelength magnetic field noise. In the ordered DFS basis [$D_{S(\pm1/2)}$, $\widetilde{D}_{0(\pm1/2)}$], the spin-trimer Hamiltonian (Eq. 1) takes the form of H_{DFS} shown in Eq. 3 which readily demonstrates the decoupling of ΔB_z from the states (see Supplementary Note S1 for the Hamiltonian represented in the full spin-trimer basis). Similarly to the bare spin-trimer case presented in Eq. 2, δj_{LR} couples $D_{S(\pm1/2)}$ and $\widetilde{D}_{0(\pm1/2)}$ states.

$$H_{\text{DFS}} = \begin{bmatrix} -\frac{3}{4}J_{12} & \frac{1}{4}\delta j_{\text{LR}} \\ \frac{1}{4}\delta j_{\text{LR}} & \frac{1}{4}J_{12} \end{bmatrix} \quad (3)$$

In general, DFS states couple equally to certain degrees of environmental fluctuations; as a result, the energy gaps between these states remain invariant to the fluctuations[11,13]. For instance, in our system, long-wavelength magnetic field fluctuations δB_{long} (Fig. 1c, blue curve), which uniformly affect the spins in the left and right sites, equally shift the energies of the states in the same m_s subspace[9,13]. In other words, the trimer states with the same m_s form a DFS protected from δB_{long} whose characteristic length scale is longer than d_{LR}. In this regard, the $D_{S(\pm1/2)}$–$D_{T(\pm1/2)}$ ($D_{S(\pm1/2)}$–$\widetilde{D}_{0(\pm1/2)}$) states form a DFS, where the corresponding energy gap $\Delta E(D_{T(\pm1/2)})$ ($\Delta E(\widetilde{D}_{0(\pm1/2)}) = E(\widetilde{D}_{0(\pm1/2)}) - E(D_{S(\pm1/2)})$) is resilient to δB_{long} as illustrated in the left panel in Fig. 1d, e.

In contrast, the short-wavelength magnetic field fluctuation δB_{short} (Fig. 1c, red curve) influences the two sites of the trimer inhomogeneously and perturbs ΔB_z in addition to the average magnetic field across the sites. Because $\Delta E(D_{T(\pm1/2)})$ is perturbed by ΔB_z, $\Delta E(D_{T(\pm1/2)})$ is prone to δB_{short}, and only $\Delta E(\widetilde{D}_{0(\pm1/2)})$ remains constant also for δB_{short}. To elucidate this, we first introduce the quantity $\langle S_L^z\rangle_A = \langle S_1^z + S_2^z\rangle_A = \langle A|S_1^z + S_2^z|A\rangle$ ($\langle S_R^z\rangle_A = \langle S_3^z\rangle_A = \langle A|S_3^z|A\rangle$), which quantifies the average z-axis spin value of the spins residing in the left (right) site for a state A. For instance, $D_{S(+1/2)} = |S\rangle|\uparrow\rangle$, and $\widetilde{D}_{0(+1/2)} = |T_0\rangle|\uparrow\rangle$ have $\langle S_L^z\rangle_{DS(+1/2)} = \langle S_L^z\rangle_{\widetilde{D}0(+1/2)} = 0$ and $\langle S_R^z\rangle_{DS(+1/2)} = \langle S_R^z\rangle_{\widetilde{D}0(+1/2)} = +1/2$; that is, $\delta\langle S_L^z\rangle_{\widetilde{D}0(+1/2)} = \langle S_L^z\rangle_{\widetilde{D}0(+1/2)} - \langle S_L^z\rangle_{DS(+1/2)} = 0$ and $\delta\langle S_R^z\rangle_{\widetilde{D}0(+1/2)} = \langle S_R^z\rangle_{\widetilde{D}0(+1/2)} - \langle S_R^z\rangle_{DS(+1/2)} = 0$. $\delta\langle S_L^z\rangle_{A(ms)} = \delta\langle S_R^z\rangle_{A(ms)} = 0$ implies that $A_{(ms)}$ and $D_{S(ms)}$ shift equally in energy with respect to the local magnetic field fluctuation in the left and right sites, and therefore, the energy gap is decoupled from δB_{short}. In this regard, $\delta\langle S_L^z\rangle_{A(ms)}$ ($\delta\langle S_R^z\rangle_{A(ms)}$) quantifies the susceptibility of the $A_{(ms)}$-$D_{S(ms)}$ gap to the local magnetic fluctuation in the left (right) site. However, because $D_{T(+1/2)}$ ($D_{T(-1/2)}$) consists of a coherent mixture of $|T_0\rangle|\uparrow\rangle$ ($|T_0\rangle|\downarrow\rangle$) and $|T_+\rangle|\downarrow\rangle$($|T_-\rangle|\uparrow\rangle$), both $\delta\langle S_L^z\rangle_{DT(\pm1/2)}$ and $\delta\langle S_R^z\rangle_{DT(\pm1/2)}$ are non-zero, implying that $\Delta E(D_{T(\pm1/2)})$ is vulnerable to δB_{short}.

In Fig. 1f, we illustrate the eigenspectrum of the trimer as a function of $\Delta B_z/J_{LR}$ calculated from Eqn. 1 with $J_{LR} = 0.1J_{12}$ and $\delta j_{LR} = 0.05J_{12}$. As expected, $\Delta E(D_{T(\pm1/2)})$ exhibits a finite slope about ΔB_z i.e., $|\partial\Delta E(\widetilde{D}_{0(\pm1/2)})/\partial\Delta B_z| > 0$ for $\Delta B_z < J_{LR}$. However, as ΔB_z is increased, $\Delta E(\widetilde{D}_{0(\pm1/2)})$ converges to J_{12}, and $\partial\Delta E(\widetilde{D}_{0(\pm1/2)})/\partial\Delta B_z$ approaches 0, which implies protection against δB_{short}. Analytically, $\Delta E(\widetilde{D}_{0(\pm1/2)}) \sim J_{12} \pm J_{LR}^2/(2\Delta B_z) + O(1/\Delta B_z^2)$ is derived from Eq. 1 for $\Delta B_z \gg J_{LR}$, illustrating that the energy gap is insensitive to ΔB_z to the first order. In Supplementary Note S2 we calculate partial derivative of $\Delta E(\widetilde{D}_{0(\pm1/2)})$ with respect to ΔB_z to demonstrate the robustness of the DFS energy gaps. We further show $\delta\langle S_L^z\rangle$ ($\delta\langle S_R^z\rangle$) for the different trimer eigenstates as a function of $\Delta B_z/J_{LR}$ in Fig. 1g, h. As expected, $\delta\langle S_L^z\rangle_{\widetilde{D}0(\pm1/2)}$ and $\delta\langle S_R^z\rangle_{\widetilde{D}0(\pm1/2)}$ approach 0 for large $\Delta B_z/J_{LR}$ (red shaded box), which reflects decoupling from δB_{short}.

Heisenberg spin-1/2 trimer in a semiconductor double quantum dot

Experimentally, we utilize a gate-defined semiconductor DQD to host the aforementioned Heisenberg spin-1/2 trimer. Figure 2a shows a scanning electron micrograph of the GaAs QD device employed in this work[23] (see "Methods"). The device was placed in a dilution refrigerator with a base temperature of 20 mK with a resulting electron temperature of T_e ~230 mK. A variable in-plane magnetic field B_{ext} was applied in the direction indicated by the white arrow. With the two-dimensional electron gas residing ~70 nm below the surface, QDs can be defined by the gate voltages[33]. In this work, we focus on the right DQD (green dots) and the single-electron transistor (SET) charge sensor on the right (yellow dot) by grounding the irrelevant gates. With this SET, we perform the high-bandwidth radio frequency (rf) reflectometry detection of the DQD charge state[34].

When two particles are confined in a QD, the Coulomb correlation between the particles become more significant in a larger QD[19,21,22]. While the orbital splitting of a QD is usually given by the confinement energy, a strong Coulomb correlation in a large QD renormalizes the orbital states and quenches the orbital splitting (or singlet-triplet splitting) of the QD[19,21,22]. Additionally, anisotropic QD confinement promotes Wigner molecularizations and further decreases the orbital splitting[22]. In our DQD, to time-resolve the electron tunneling events between the right QD and its reservoir, the QD is tuned less transparent compared to the left one implying that the left QD has a larger QD radius. Moreover, we find the left QD confinement is anisotropic[23], which fosters Wigner-molecularization. This leads to small orbital splitting $\delta L_{ST} < 10$ GHz·h, which is also gate-voltage tunable, despite the relatively small Coulomb correlation effect in GaAs[22]. We note that such anisotropy can be further tailored through lithographic design, enabling consistent and controllable Wigner molecularization in QDs[24,35]. In contrast, a negligible correlation effect in the right QD results in a large orbital splitting of the QD, δR_{ST} ~ 108 GHz·h (right panel in Fig. 2a), which is estimated by pulsed-gate spectroscopy[36] (see Supplementary Note S3).

The DQD is operated in the [2,1]–[1,2] charge configuration to define the Heisenberg spin-1/2 trimer. Here, n (m) denotes the number of electrons in the left (right) QD by [n,m] notation. Figure 2b presents the relevant

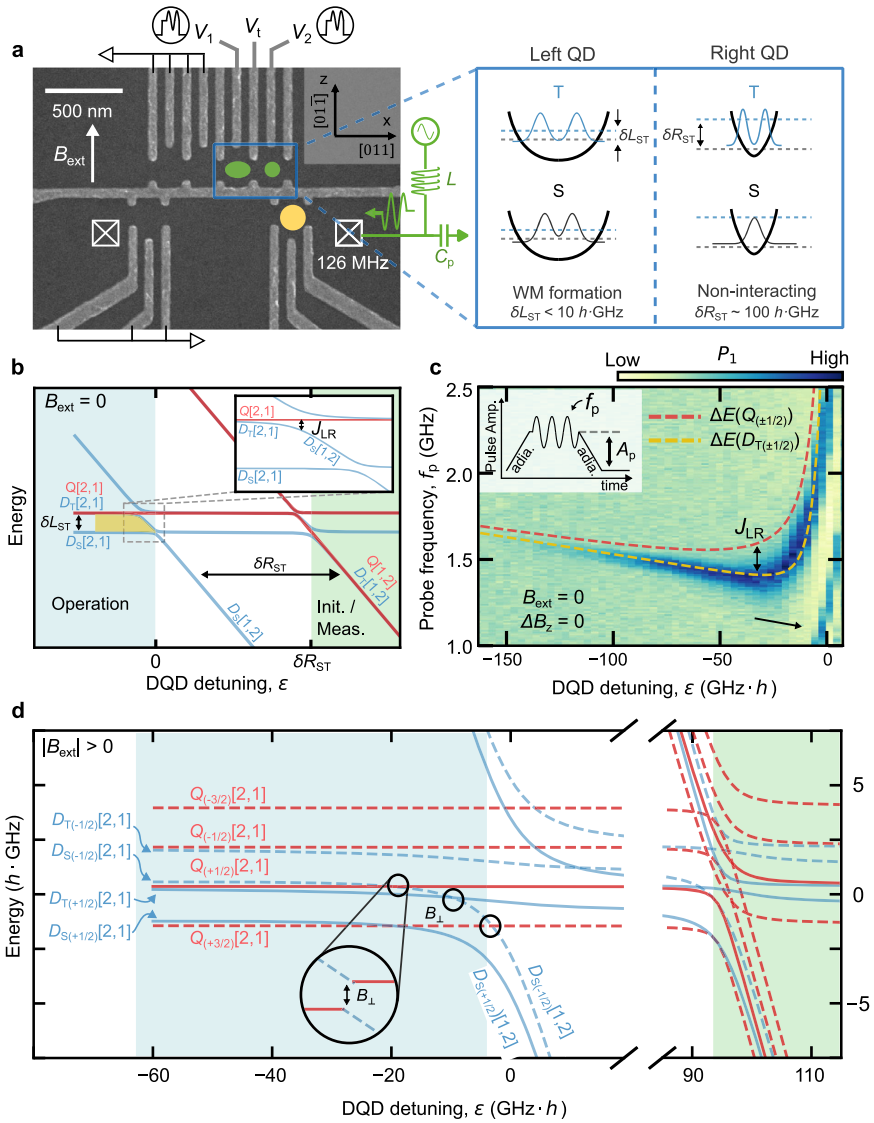

Fig. 2 | Heisenberg spin-trimer in a gate-defined semiconductor double quantum dot. a Scanning electron microscopy of the GaAs quantum dot (QD) device used in this work. The green dots denote the double QD (DQD) hosting a three-electron Heisenberg trimer aligned along the [011] crystal axis. As illustrated in the right panel, the left (right) QD confinement potential promotes (prevents) the formation of a Wigner molecule (WM), resulting in a small (large) orbital splitting δL_{ST} (δR_{ST}) in the left (right) QD. The yellow dot depicts a radio-frequency single-electron transistor (rf-SET) charge sensor. An LC tank circuit is attached to the ohmic contact close to the rf-SET. An external magnetic field B_{ext} is applied along the white arrow. **b** Eigenenergy spectrum of a three-electron system in a DQD at $B_{ext} = \Delta B_z = 0$. The corresponding energies along the [2,1]-[1,2] charge configurations are presented as a function of DQD detuning, ε, with small (large) δL_{ST} (δR_{ST}). Inset: Zoom-in of the energy diagram near $\varepsilon = 0$. J_{LR} represents the inter-QD exchange interaction. **c** Pulsed-microwave spectroscopy of the trimer at [2,1] at $B_{ext} = 0$. The probability of the excited orbital state, P_1 is shown as a function of the applied microwave probe frequency f_p, and ε (see inset for the pulse schematic. A_p is the amplitude of the detuning pulse.)⊡ The yellow (red) dashed curves illustrate the $D_{T(\pm1/2)}$-$D_{S(\pm1/2)}$ ($Q_{(\pm1/2)}$-$D_{S(\pm1/2)}$) energy gap calculated from the three-electron Hamiltonian (Supplementary Note S4). The black arrow denotes the transition driven by the two-photon process. **d** Eigenspectrum at $|B_{ext}| > 0$ as a function of ε. The black circles denote avoided crossings between states with different m_s due to the finite transverse nuclear Overhauser field $B^\perp$. Inset: Zoom-in of the $B^\perp$ avoided-crossing between $D_{S(-1/2)}[2,1]$ and $Q_{(+1/2)}[2,1]$.

energy diagram as a function of the DQD detuning ε, at $B_{ext} = \Delta B_z = 0$ (We naturally adopt $\Delta B_z = B_z^L - B_z^R$ from Fig. 1, defining B_z^L (B_z^R) as the local magnetic field at the left (right) QD.). In a deep-detuned [2,1] or [1,2] regime, where the direct charge transitions between the QDs are inhibited, the system can be described by the anti-ferromagnetic Heisenberg Hamiltonian presented in Eq. 1[9]. In particular, the [2,1] configuration is identical to the case presented in Fig. 1a with $J_{12} \gg J_{LR}$ where J_{12} is now dominated by δL_{ST}. Thereby in [2,1], when two electrons in the left QD form a spin-singlet and occupy the ground orbital, the trimer state becomes a $D_{S(\pm1/2)}[2,1]$. $A_{(ms)}[n,m]$ denotes the corresponding spin and DQD charge state simultaneously. However, if the two electrons in the left QD form a spin-triplet and occupy the excited orbital, the trimer state can be either a $D_{T(\pm1/2)}[2,1]$ or a quadruplet state ($Q_{(\pm1/2)}[2,1]$ or $Q_{(\pm3/2)}[2,1]$) depending on S_{tot}.

Furthermore, in our DQD system, J_{23} (J_{31}) corresponds to the exchange interaction between the ground (excited) state of the left QD and the ground state of the right QD[9]. The strength of J_{23} (J_{31}) can be derived using Schrieffer–Wolff transformation which yields $J_{23} = \frac{2t_{SS}^2}{\varepsilon}$ ($J_{31} = \frac{2t_{TS}^2}{\varepsilon - \Delta E(\varepsilon)}$)[9]. Here, t_{ij} denotes the tunnel coupling strength between the i orbital state in the left QD and the j orbital state in the right QD (see Supplementary Note S4), and $\Delta E(\varepsilon)$ is the energy splitting between the ground and excited state in the left QD which depends on ε[9].

At $\varepsilon > \delta R_{ST}$ (green shaded region in Fig. 2b) if the Fermi-level of the reservoir lies in between the ground and excited orbital levels, only the electron from an excited orbital ($D_{T(\pm1/2)}[1,2]$, $Q_{(\pm1/2)}[1,2]$, or $Q_{(\pm3/2)}[1,2]$) can tunnel out to the reservoir and tunnel back in to fill the ground state $D_{S(\pm1/2)}[1,2]$, known as the energy-selective tunneling (EST) process[23,37,38]. With $\delta R_{ST} \sim 108$ GHz·$h > 50 k_B T_e$ (k_B is the Boltzmann constant), the rf-SET in our device allows the time-resolved detection of such EST, allowing the single-shot measurement of the trimer states[23].

Based on the EST readout, we explore the excitation spectrum of the trimer in the [2,1] configuration at $B_{ext} = \Delta B_z = 0$ by pulsed-microwave spectroscopy[39]. For the spectroscopy, we first initialize the spin state to $D_{S(\pm1/2)}[1,2]$ at $\varepsilon_{init} > \delta R_{ST}$ exploiting the EST[23]. By pulsing the initialized state into the [2,1] configuration adiabatically with respect to the inter-dot tunnel coupling rate, we transfer $D_{S(\pm1/2)}[1,2]$ to $D_{S(\pm1/2)}[2,1]$. Then, we apply an electric microwave tone to gate V_1 (Fig. 2a), which excites $D_{S(\pm1/2)}[2,1]$ to $D_{T(\pm1/2)}[2,1]$ if the frequency of the tone matches $\Delta E(D_{T(\pm1/2)})/h$. The $D_{T(\pm1/2)}[2,1]$ population can be detected via the EST process, once adiabatically brought back to $D_{T(\pm1/2)}[1,2]$ at ε_{init}. Figure 2c shows the resulting $D_{T(\pm1/2)}[2,1]$ population as a function of the microwave frequency f_p and ε, which reveals the degenerate spectrum corresponding to $\Delta E(D_{T(+1/2)}[2,1]) = \Delta E(D_{T(-1/2)}[2,1])$. The pulse amplitude $A_p = \varepsilon_p - \varepsilon_{init}$ (schematic in Fig. 2c) is varied to sweep over ε. Here, the pulse-tip ε_p is the DQD detuning reached by the pulse. The yellow (red) dashed curve superposed onto Fig. 2c corresponds to $\Delta E(D_{T(\pm1/2)}[2,1])$ ($\Delta E(Q_{(\pm1/2)}[2,1]) = \Delta E(Q_{(\pm3/2)}[2,1])$) calculated from our three-electron DQD Hamiltonian (see Supplementary

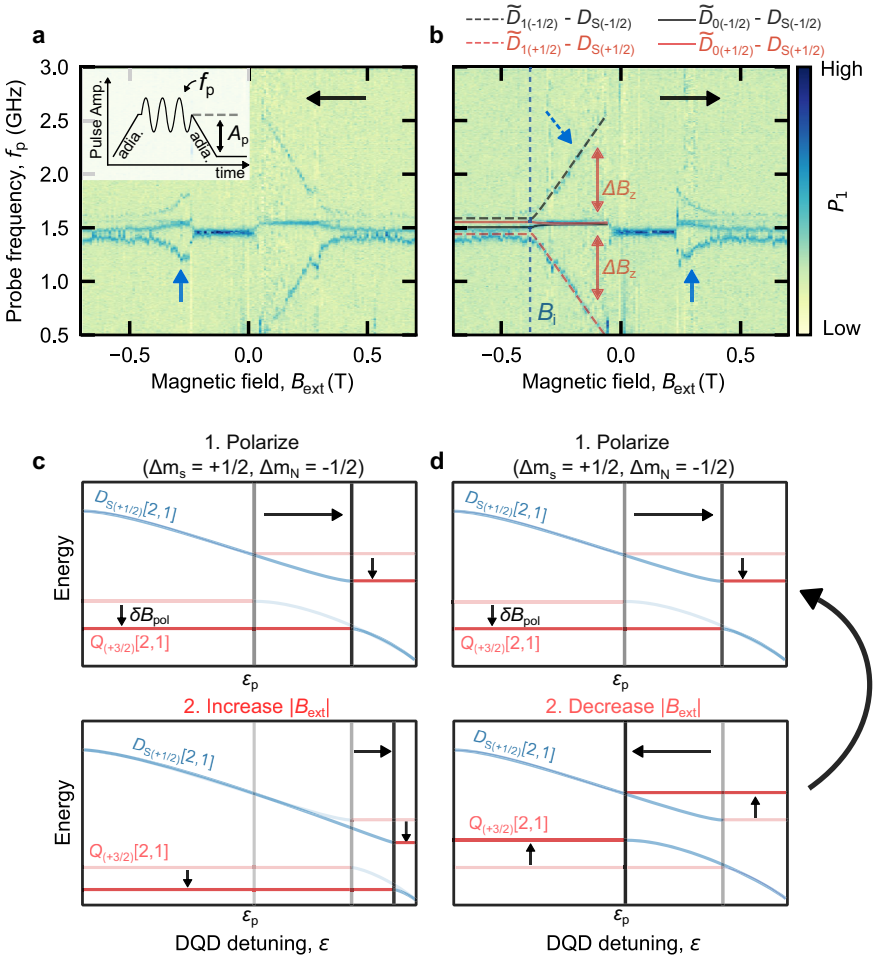

Fig. 3 | Spectrum of a spin-trimer under a varying magnetic field gradient. a, **b** Magnetospectroscopy of the trimer with decreasing (increasing) B_{ext}. Excited orbital state probability P_1 is recorded as a function of f_p and B_{ext}, with constant A_p (see inset to **a** for the pulse schematics). The black arrow illustrates the B_{ext} sweep direction. Pulse-induced DNP (see Supplementary Note S5) builds hysteretic ΔB_z about the sweep direction and leads to the four different transitions presented. The black (red) solid and dashed lines represent the $\widetilde{D}_0$–D_S and $\widetilde{D}_1$–D_S energy splitting in $m_s = -1/2$ ($m_s = 1/2$) subspace, respectively, calculated from the toy-model Hamiltonian together with varying ΔB_z (see Supplementary Note S4). **c** Schematic of the pulse-induced DNP process for increasing $|B_{ext}|$. Top panel: when the pulse tip, ε_p, coincides with the $B^{\perp}$ avoided-crossing, DNP is facilitated to increase the electron Zeeman splitting by δB_{pol}, and shifts the avoided-crossing to a more positive ε. Bottom panel: Increasing $|B_{ext}|$ shifts the avoided-crossing to more positive ε, prohibiting additional DNP. This results in the DNP in a limited region (solid blue arrows in (**a**, **b**)). **d** Schematic of the pulsed induced DNP process for decreasing $|B_{ext}|$. Top panel: the DNP shifts the $B^{\perp}$ avoided-crossing to a more positive ε as shown in **c**. Bottom panel: Decreasing $|B_{ext}|$ refocuses the avoided-crossing to ε_p, which enables additional DNP.

Note S4). We empirically find $\delta L_{ST} \sim 1.3$ GHz·h, which is an order of magnitude smaller than the orbital splitting ~70 GHz·h expected from the lithographic size of the QD. This confirms the Wigner-molecularization in the left QD. The transitions from $D_{S(\pm1/2)}[2,1]$ to $Q_{(\pm1/2)}[2,1]$ or to $Q_{(\pm3/2)}[2,1]$ (red dashed curve in Fig. 2c) are prohibited due to the spin selection rule[9]; hence, these transitions are not visible on the measured spectrum. $D_{S(\pm1/2)}[2,1]$ – $D_{T(\pm1/2)}[2,1]$ forms a basis for the spin-charge hybrid qubit, where $\Delta E(D_{T(\pm1/2)}[2,1])$ exhibits a smaller slope with respect to ε compared to a bare charge qubit transition, resulting in reduced charge noise sensitivity[9,40]. Furthermore, the energy difference between $Q_{(\pm1/2)}[2,1]$ and $D_{T(\pm1/2)}[2,1]$ is proportional to J_{LR} which varies with ε. Below, only the trimer states in the [2,1] configuration are discussed and the charge states are omitted from the notation.

For $|B_{ext}| > 0$, the D_S and D_T states split into $m_s = -1/2, +1/2$, and the Q state splits into $m_s = -3/2, -1/2, +1/2, +3/2$ states (Fig. 2d). When the states with different m_s become degenerate due to Zeeman splitting, the degeneracy is lifted by the transverse nuclear Overhauser field $B^{\perp}$ and results in an avoided-crossing between the states with $|\Delta m_s| = 1$[24,41]. These avoided-crossings are marked by black circles in Fig. 2d. Finite $B^{\perp}$ allows DNP processes which also builds $\Delta B_z > 0$[24,41,42](see Supplementary Note S5).

Spectroscopy of the spin trimer under finite ΔB_z

Figure 3a, b show the magnetospectroscopy of the trimer with different B_{ext} sweep directions. For the spectroscopy, a microwave tone is superposed to the polarization phase of the DNP pulse shown in Supplementary Note S5, implying the pulse is also capable of DNP. Here, we keep the pulse detuning amplitude $A_p \sim 200$ GHz·h to reach $\varepsilon = \varepsilon_p \sim -70$ GHz·h in the [2,1] configuration. Here, $\Delta E(D_{T(\pm1/2)}) \sim J_{12} \sim 1.45$ GHz·h and $J_{LR} \sim 0.17$ GHz·h present the relevant energy scales. From the toy-model Hamiltonian parameters (see Supplementary Note S4), we also obtain $J_{23} \sim 0.138$ GHz·h and $J_{31} \sim 0.197$ GHz·h, yielding $\delta j_{LR} \sim 0.06$ GHz·h. As B_{ext} is increased from 0 to 231.5 mT to match $(g^*\mu_B)B_{ext} = \Delta E(D_{T(\pm1/2)})$ (Fig. 3b), from which we extract $|g^*| \sim 0.44$[43], $D_{S(-1/2)}$ becomes degenerate with $D_{T(+1/2)}$ at ε_p due to the Zeeman splitting, and DNP occurs. As a consequence, the finite ΔB_z due to the DNP mixes $D_{T(+1/2)}$ ($D_{T(-1/2)}$) and $Q_{(+1/2)}$ ($Q_{(-1/2)}$) where $D_{S(+1/2)}$ ($D_{S(-1/2)}$) can now be electrically excited to both mixtures as discussed above. This explains the four transitions viable in the spectrum for $B_{ext} > \Delta E(D_{T(\pm1/2)})$.

The DNP yields a highly hysteretic spectrum depending on the field sweep direction. If ε_p coincides with a $B^{\perp}$ avoided-crossing, the DNP increases the size of the Zeeman splitting which shifts the avoided-crossing to more positive ε (Fig. 3c, top panel). A further increase in $|B_{ext}|$ in the next sweep step shifts the crossing to an even more positive ε, prohibiting additional DNP (Fig. 3c, bottom panel). Consequently, while increasing $|B_{ext}|$, the pulse can induce DNP within a small B_{ext} window (near the blue solid arrows in Fig. 3a, b). This results in a small ΔB_z, which eventually decays as a function of time. In contrast, when decreasing $|B_{ext}|$, even though the DNP shifts the avoided-crossing towards positive ε (Fig. 3d, top panel), decreasing $|B_{ext}|$ re-focuses the crossing to ε_p, allowing additional DNP (Fig. 3d, bottom panel). We note that such re-focusing is possible because the relaxation time of the Overhauser field (~10^0 min[24]) is longer than the time required to decrease $|B_{ext}|$ by one sweep step (~10 s). In other words, when decreasing $|B_{ext}|$, the DNP translates the decreased B_{ext} into the Overhauser field to preserve the constant Zeeman splitting experienced by the electrons, and maintains the $B^{\perp}$ avoided-crossing at ε_p. This allows the DNP to persist over a large range of B_{ext}, and yields large $\Delta B_z \sim 1.05$ GHz·h

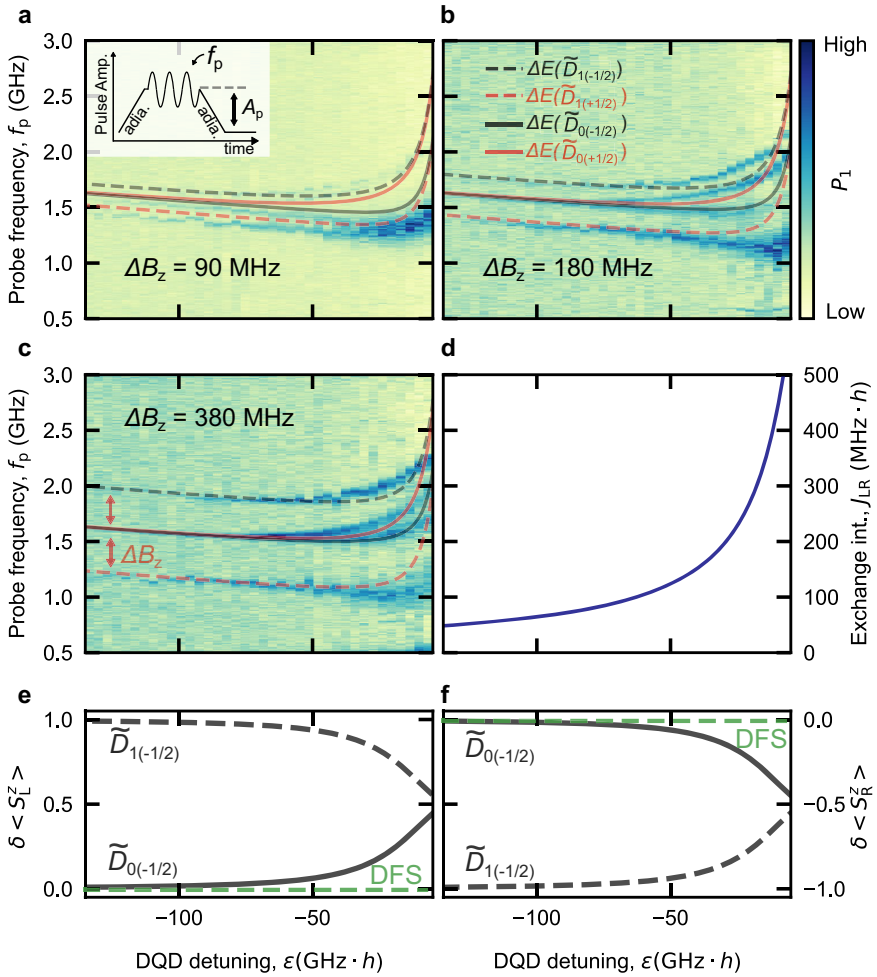

Fig. 4 | Spectrum of a spin-trimer under varying inter-QD exchange interaction strengths. **a**–**c** Pulsed microwave spectroscopy of the trimer along the DQD detuning ε for ΔB_z = 90, 180, and 380 MHz·h. Excited orbital state population P_1 is recorded as a function of the microwave probe frequency f_p and ε for each panel. The superposed lines correspond to the energy spectrum calculated from the toy-model Hamiltonian with the respective ΔB_z (see Supplementary Note S2). Inset to **a**: Schematic of the pulse utilized for the spectroscopy. **d** Inter-QD exchange interaction strength J_{LR} as a function of ε, evaluated from the Hamiltonian. **e**, **f** Susceptibility of the energy gap to magnetic field fluctuation in the left (right) QD as a function of ε. For the calculation, $J_{LR}(\varepsilon)$ shown in (**d**) is assumed with ΔB_z = 380 MHz·h. $\delta\langle S_L^z\rangle = 0$ ($\delta\langle S_R^z\rangle = 0$), represented by the green dashed line, implies the decoupling of the relevant energy gaps from the local magnetic field fluctuation in the left (right) QD.

(red arrows in Fig. 3b), corresponding to $\Delta B_z/J_{LR} \sim 6.17$. Moreover, although the quenching of ΔB_z at low $|B_{ext}|$ suggests that a minimum $|B_{ext}|$ is required to maintain the polarization of the nuclear spins, detailed investigations are required to verify the quenching mechanism.

The red (black) solid and dashed lines in Fig. 3b denote the energy splittings in the $m_s = +1/2$ ($m_s = -1/2$) subspace calculated from the toy-model Hamiltonian with finite ΔB_z. For the calculation, $\Delta B_z \sim 50$ MHz is assumed in the range $B_{ext} = -700$ mT $\sim B_i$, where we suppose that DNP becomes effective for $|B_{ext}| < |B_i|$ to linearly build ΔB_z up to ~1.05 GHz·h. Noting that B_{ext} is translated into the Overhauser field when decreasing $|B_{ext}|$, the slope ~0.53 (denoted by the blue-dashed arrow in Fig. 3b) infers the effectiveness of our DNP in building ΔB_z. As illustrated in Fig. 1f, the excitation spectra in the $m_s = \pm 1/2$ subspace asymptotically approach $\Delta E(\widetilde{D}_{0(\pm 1/2)})$ and $\Delta E(\widetilde{D}_{1(\pm 1/2)})$ for large ΔB_z, reaching the "true" DFS formed by $D_{S(\pm 1/2)}$ and $\widetilde{D}_{0(\pm 1/2)}$. While the finite magnetic field gradient within the left QD hosting the WM, $\delta b_{z,L}$ may lead to additional modulation of $\Delta E(\widetilde{D}_{0(\pm 1/2)})$, we show that the DNP does not introduce significant $\delta b_{z,L}$, and that the DFS is still protected from the fluctuation in ΔB_z even under a finite $\delta b_{z,L}$ via numerical calculations in Supplementary Note S2. We also demonstrate that the partial derivative of $\Delta E(\widetilde{D}_{0(\pm 1/2)})$ with respect to $\delta b_{z,L}$ is also suppressed when $\delta b_{z,L} \sim 0$ (see Supplementary Note S2).

Although Fig. 3 readily demonstrates the modulation of the eigenspectrum under $\Delta B_z \gg J_{LR}$, we additionally vary J_{LR} with ε and show the resulting eigenspectrum in Fig. 4. Figure 4a–c present the pulsed microwave spectra of the trimer spanned by ε and f_p, at different ΔB_z. To generate finite ΔB_z, we perform the magnetospectroscopy shown in Fig. 3a, b by decreasing $|B_{ext}|$ from a large value and stopping at a certain value. From our toy-model Hamiltonian, we calculate the eigenspectrum as a function of ε at constant ΔB_z, plotted in Fig. 4a–c (see Supplementary Note S2), where we estimate ΔB_z = 80 (180 and 380) MHz·h for Fig. 4a, b, c by empirically fitting to the eigenspectrum. We note the simulated spectra may deviate from the observations due to the nuclear spin diffusion during the measurements[44].

As shown in Fig. 4d, $J_{LR}(\varepsilon)$ decays as ε is more negatively detuned (Fig. 2b, c). Consequently, for a fixed ΔB_z, the ratio $\Delta B_z/J_{LR}$ increases for negative detuning, where the "true" DFS emerges. We further evaluate $\delta\langle S_L^z\rangle$ ($\delta\langle S_R^z\rangle$) in Fig. 4e, f as a function of ε, assuming ΔB_z = 380 MHz·h. Evidently, both $\delta\langle S_L^z\rangle_{\widetilde{D0(-1/2)}}$ and $\delta\langle S_R^z\rangle_{\widetilde{D0(-1/2)}}$ approach 0 for large detuning, implying protection against δB_{short}.

We further probe the trimer by coherent Landau-Zener-Stückelberg (LZS) oscillation with different B_{ext} sweep directions (Fig. 5a, b). The corresponding fast-Fourier-transformations (FFTs) are shown in Fig. 5c, d, respectively. Here non-adiabatic square pulses with varying length τ and with a fixed amplitude are applied to induce LZS oscillation[24,40]. These LZS pulses can similarly result in DNP when the pulse tip matches the degeneracy as in Fig. 3a, b, which in turn reveals ΔB_z split states evident from the FFT.

Compared to the four clear transitions shown in Fig. 3a, b, however, two branches are faintly visible on the LZS spectrum even though two energy levels are accessible for each $D_{S(+1/2)}$ and $D_{S(-1/2)}$. We ascribe this to the negligible Landau-Zener transition probability to the upper excited state for each m_s subspace due to the finite rise-time of the LZS pulses[45]. Explicitly, if the state is initialized to $D_{S(+1/2)}$ ($D_{S(-1/2)}$), the LZS oscillation mainly reveals the phase oscillation corresponding to $\Delta E(\widetilde{D}_{1(+1/2)})$ ($\Delta E(\widetilde{D}_{0(-1/2)})$), which is lower in energy than $\Delta E(\widetilde{D}_{0(+1/2)})$ ($\Delta E(\widetilde{D}_{1(-1/2)})$), as shown in

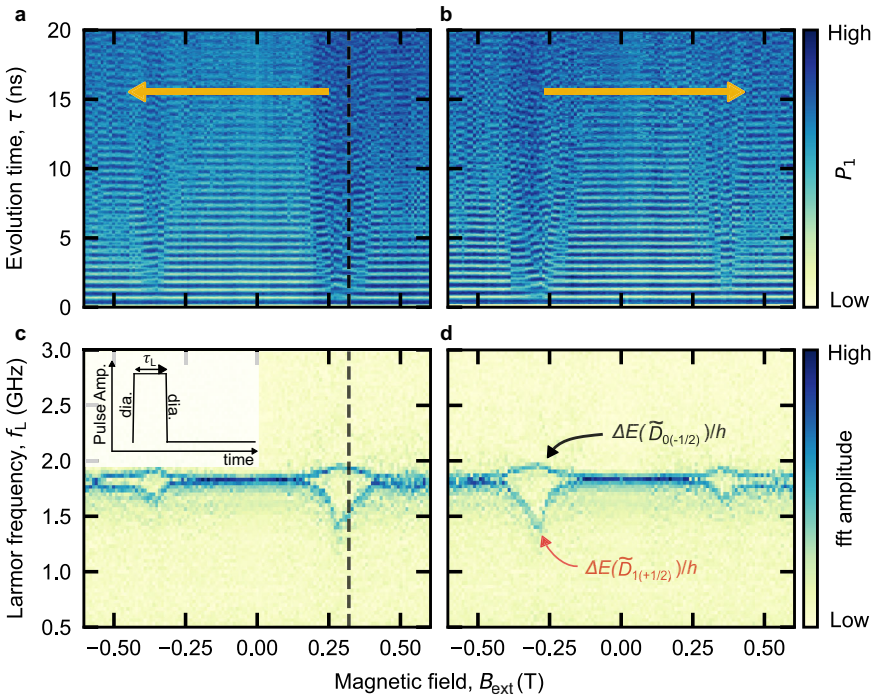

Fig. 5 | Landau–Zener–Stückelberg oscillation of a spin-trimer. a, **b** Landau–Zener–Stückelberg (LZS) oscillation of the trimer with decreasing (increasing) B_{ext}. Excited orbital state population P_1 is recorded as a function of the free evolution time τ (see inset to **c** for the pulse schematic), and B_{ext}. **c**, **d** Fast-Fourier-transformation (FFT) of the LZS oscillation shown in (**a** (**b**)). The LZS pulse-induced DNP builds finite ΔB_z and results in the two distinct frequencies related to $\Delta E(\widetilde{D}_{0(-1/2)})$ and ΔE $(\widetilde{D}_{1(+1/2)})$. The Larmor frequencies corresponding to $\Delta E(\widetilde{D}_{0(+1/2)})$ and ΔE $(\widetilde{D}_{1(-1/2)})$ are not visible due to the small Landau-Zener transition given by the finite rise time of the pulse.

Fig. 1f. Moreover, the effect of DNP is less prominent with this pulsing scheme compared to the case in Fig. 3a, b because average time pulse spends at the $B^{\perp}$ avoided-crossing is shorter in this measurement sequence.

Real-time Bayesian estimation of the spin trimer energy splitting

Based on the coherent LZS oscillation we further investigate the real-time fluctuation of the energy levels by Bayesian Hamiltonian estimation[29–31]. By applying 300 different LZS pulses with the linearly increasing pulse durations $\tau_i = i\tau_1 (1 \le i \le 300)$ and evaluating the corresponding measurement outcome m_i after each pulse, the estimator evaluates the probability density $P\left(\Delta E\left(\widetilde{D}_{0(-1/2)}\right)/h, \Delta E\left(\widetilde{D}_{1(+1/2)}\right)/h | m_1, m_2 \ldots m_{300}\right)$ based on the Bayes theorem. Two different frequencies maximizing the probability density, $\Delta E(\widetilde{D}_{0(-1/2)}; t)/h$ and $\Delta E(\widetilde{D}_{1(+1/2)}; t)/h$, indicate the corresponding LZS oscillation frequencies at a certain laboratory time t (see "Methods" for details of the Bayesian estimation). Figure 6a shows the estimated frequencies as a function of the laboratory time. Here, each single-shot measurement takes ~20 μs, implying ~6 ms per estimation.

Figure 6b presents the histograms of the time traces shown in Fig. 6a. From the histogram we extract the standard deviations of $\Delta E(\widetilde{D}_{0(-1/2)})/h$ and $\Delta E(\widetilde{D}_{1(+1/2)})/h$, $\sigma_{\widetilde{D0(-1/2)}}$ and $\sigma_{\widetilde{D1(+1/2)}}$, respectively. Notably, $\sigma_{\widetilde{D0(-1/2)}}$ is significantly smaller than $\sigma_{\widetilde{D1(+1/2)}}$. This clearly demonstrates the protection against δB_{short} for $\Delta E(\widetilde{D}_{0(-1/2)})$ in comparison to $\Delta E(\widetilde{D}_{1(+1/2)})$. Figure 6c additionally shows the variance, σ^2, along time interval T over which the variance is evaluated[29,46]. Compared to the standard diffusion case (blue dashed line), where the variance increases linearly with T, the variances of $\sigma^2_{\widetilde{D1(+1/2)}}$ (red circles) and $\sigma^2_{\widetilde{D0(-1/2)}}$ (black circles) show $\sigma^2 \sim DT^{\alpha}$ with $\alpha<1$, and the diffusion coefficient D. This indicates the sub-diffusive behavior of the energy splittings, where we extract $\alpha=0.50$ ($\alpha = 0.055$) for $\Delta E(\widetilde{D}_{1(+1/2)})/h$ ($\Delta E(\widetilde{D}_{0(-1/2)})/h$). The small α suggests that the states are mainly affected by a non-Gaussian noise correlator[47], implying the states are less affected by the nuclear spin diffusion, which is assumed to be a typical Gaussian noise correlator[29,44].

Time traces of the energy gaps at different ΔB_z and at different $J_{LR}(\varepsilon)$ are recorded to further probe the effect of $\Delta B_z/J_{LR}$ on the robustness. In Fig. 6d, which shows $\sigma_{\widetilde{D0(-1/2)}}$ and $\sigma_{\widetilde{D1(+1/2)}}$ at different $\Delta B_z/J_{LR}$, we superpose $\delta\langle S^z_L - S^z_R\rangle_{\widetilde{D1(-1/2)}} = \delta\langle S^z_1 + S^z_2 - S^z_3\rangle_{\widetilde{D1(-1/2)}}$ $(\delta\langle S^z_L - S^z_R\rangle_{\widetilde{D0(+1/2)}})$ as a function of $\Delta B_z/J_{LR}$ as a black (red) curve. $\delta\langle S^z_L - S^z_R\rangle_{A(ms)}$ quantifies the degree of protection against ΔB_z noise for the $A_{(ms)}$–$D_{S(ms)}$ gap. Here, we assume that, for minimal $\delta\langle S^z_L - S^z_R\rangle = 0$, the frequency resolution of our estimator sets the lower bound of $\sigma_{min} \sim 1$ MHz. In addition, ΔB_z fluctuation ~13.39 MHz, measured by the singlet-triplet qubit in this device (see Supplementary Note S4), sets the upper bound at the maximal $\delta\langle S^z_L - S^z_R\rangle = 2$[42]. Because the Bayesian estimation is carried out when $\Delta B_z < 200$ MHz·h, we expect smaller $\sigma_{\widetilde{D0(-1/2)}}$ for larger ΔB_z, which is indeed within reach as demonstrated in Fig. 3a, b. Thereby, we anticipate a larger ΔB_z to provide enhanced protection against δB_{short} in addition to the inherent δB_{long} resilience, which would further facilitate highly coherent spin qubit operations completely decoupled from the magnetic field noise.

Discussion

In this work, we present a "true" DFS, robust to both short- and long-wavelength magnetic field fluctuations, in an antiferromagnetic Heisenberg spin-1/2 trimer. Compared to previously proposed "true" DFSs schemes in QDs[16,17], the DFS presented here offers a more compact and practical route toward magnetic noise-free spin qubit operations. We envision a well-engineered pulse scheme, altering between the DNP and control phase, to facilitate coherent qubit control in the DFS in GaAs. Additionally, exploiting the tunability of the strongly-correlated states[24,27] the dispersion of the energy levels can be tuned to have a smaller slope about ε, which may further suppress the charge noise susceptibility.

Presented "true" DFS can be realized in DQD systems with small singlet-triplet splitting, and large ΔB_z. In this regard, the extension of the DFS scheme to group-IV materials such as Si or Ge is also expected to be feasible without requiring DNP. In Si, valley-excited states can provide access to spin triplet states[9,32] without the need for WM formation, where a micromagnet can induce a sizable ΔB_z to realize the true DFS[48,49]. Such DFS in Si may exhibit reduced susceptibility to the potential decoherence introduced by $\delta b_{z,L}$ as the charge density will not

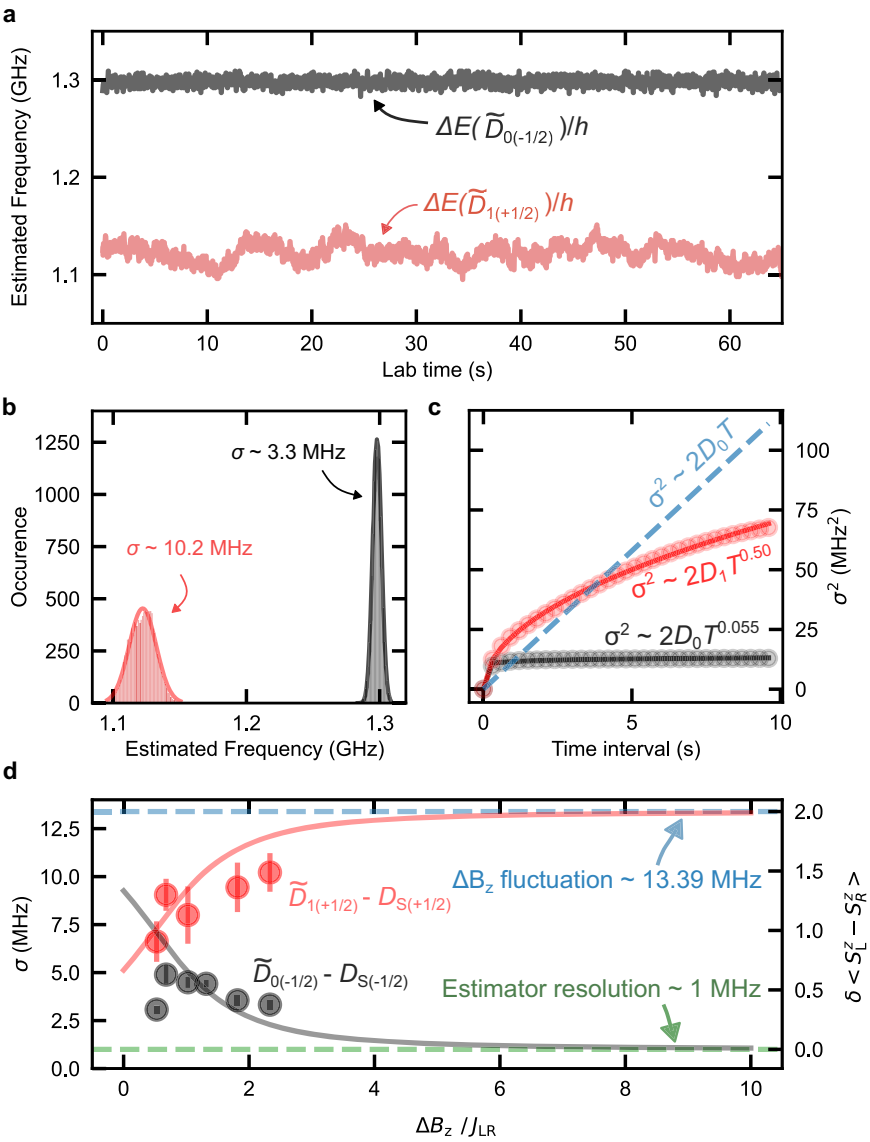

Fig. 6 | Real-time Bayesian inference of energy fluctuations. a Bayesian-estimated $\Delta E(\widetilde{D}_{0(-1/2)})/h$ [$\Delta E(\widetilde{D}_{1(+1/2)})/h$] along laboratory time shown in the black [red] trace. Both energy splittings are simultaneously estimated every 6 ms based on 300 EST single-shot measurements. **b** Histogram of the frequency fluctuation shown in **a**. Numerical fit (solid line) to a Gaussian function yields the standard deviation σ ~ 3.3 MHz [10.2 MHz] for $\Delta E(\widetilde{D}_{0(-1/2)})/h$ [$\Delta E(\widetilde{D}_{1(+1/2)})/h$] fluctuation. **c** Variance of the fluctuation σ^2 as a function of the time interval T. Numerical fit (solid line) to a sub-diffusion model $\sigma^2 = 2DT^{\alpha}$ result in D = 5.78 MHz^2/s$^{0.055}$ [11.19 MHz^2/s$^{0.5}$] and α = 0.055 [0.5] for $\Delta E(\widetilde{D}_{0(-1/2)})/h$ [$\Delta E(\widetilde{D}_{1(+1/2)})/h$] fluctuation. The blue dashed line illustrates the expected variance for a standard diffusion process with D = 5.78 MHz^2/s. **d** Standard deviation of $\Delta E(\widetilde{D}_{0(-1/2)})/h$ [$\Delta E(\widetilde{D}_{1(+1/2)})/h$] measured for different $\Delta B_z/J_{LR}$ presented as solid black (red) circles. The lower (upper) bound of the fluctuation is set by the estimator resolution ~1 MHz (standard deviation of the ΔB_z fluctuation ~13.39 MHz, see Supplementary Note S4) shown as green (blue) dashed lines. The black [red] solid curve corresponds to $\delta\langle S_L^z - S_R^z\rangle$ of $\widetilde{D}_{0(-1/2)}$ [$\widetilde{D}_{1(1/2)}$] branch as a function of $\Delta B_z/J_{LR}$.

be spatially localized in the absence of WM formation. In contrast, in Ge, WM formation remains necessary to access the triplet states as presented in this work[28]. The site-dependent and gate-tunable g-factors of holes in Ge may enable a large ΔB_z[50] for forming the true DFS. This tunability may also provide a potential route to minimize the Zeeman splitting difference between the two holes forming the WM. Overall, these implementations in Si or Ge alleviate the need for DNP phase to maintain ΔB_z and support scalable qubit control schemes in the presented DFS, which may ultimately enable the operations of multiple qubits residing in the DFS.

Methods

Device fabrication

A quadruple QD device was fabricated on a GaAs/AlGaAs heterostructure with a two-dimensional electron gas (2DEG) formed ~70 nm below the surface. An electronic mesa near the QD array was defined by wet etching leaving the 2DEG only around the QDs. A metal stack of Ni/Ge/Au was thermally diffused into the mesa to form the ohmic contacts. Metal gates for QD formation were defined by the standard electron-beam lithography and evaporation technique (5 nm Ti/30 nm Au). Course gate structures including the bonding pads were deposited using photolithography and evaporation (5 nm Ti/200 nm Au).

Eigenspectrum of the Heisenberg spin trimer at different ΔB_z

We show the explicit spin expressions for the eigenstates of the Heisenberg spin trimer (Eqn. 1) at $\Delta B_z = 0$ (Table 1) and at $|\Delta B_z| \gg J_{LR}$ (Table 2). In each table, the state in the first (second) bracket refers to the two- (single-) spin state in the left (right) site. The spin triplet states T_0, T_+, T_- correspond to $(|\uparrow\downarrow\rangle + |\downarrow\uparrow\rangle)/\sqrt{2}$, $|\uparrow\uparrow\rangle$, and $|\downarrow\downarrow\rangle$, respectively, and S denotes the spin singlet state, $(|\uparrow\downarrow\rangle - |\downarrow\uparrow\rangle)/\sqrt{2}$.

Bayesian estimation

To record the fluctuation of the Heisenberg spin trimer eigenstates, we perform Bayesian Hamiltonian estimation[29–31] based on energy selective tunneling (EST) single-shot state detection[23,37,38]. For the estimation, we apply N = 300 different LZS pulses (see Fig. 5) with the nth pulse having the free evolution time $\tau_n = n \cdot t_1 = n \cdot 0.12$ ns, where each pulse is followed by a single-shot readout. Because the LZS pulse mainly reveals the coherent oscillation between $D_{S(+1/2)}-\widetilde{D}_{1(+1/2)}$ and $D_{S(-1/2)}-\widetilde{D}_{0(-1/2)}$ (Fig. 5) the probability of measuring the excited (ground) state at the nth measurement is given by $P(M_n = e|f_1, f_2) = \alpha + \beta_1 \sin(2\pi f_1 \tau_n) + \beta_2 \sin(2\pi f_2 \tau_n)$ ($P(M_n = g|f_1, f_2) = 1 - P(M_n = e|f_1, f_2)$). Here f_1 and f_2 are the oscillation frequencies corresponding to the $D_{S(+1/2)}-\widetilde{D}_{1(+1/2)}$ and $D_{S(-1/2)}-\widetilde{D}_{0(-1/2)}$ oscillations, respectively, and M_n is the nth measurement result which can be either the

Table. 1 | Eigenstates of the Heisenberg spin trimer at $\Delta B_z = 0$

State	Spin expression
$Q_{(+3/2)}$	$\|T_+\rangle\|\uparrow\rangle$
$Q_{(+1/2)}$	$\frac{1}{\sqrt{3}}[\sqrt{2}\|T_0\rangle\|\uparrow\rangle + \|T_+\rangle\|\downarrow\rangle]$
$Q_{(-1/2)}$	$\frac{1}{\sqrt{3}}[\sqrt{2}\|T_0\rangle\|\downarrow\rangle + \|T_-\rangle\|\uparrow\rangle]$
$Q_{(-3/2)}$	$\|T_-\rangle\|\downarrow\rangle$
$D_{S(+1/2)}$	$\|S\rangle\|\uparrow\rangle$
$D_{T(+1/2)}$	$\frac{1}{\sqrt{3}}[\|T_0\rangle\|\uparrow\rangle - \sqrt{2}\|T_+\rangle\|\downarrow\rangle]$
$D_{S(-1/2)}$	$\|S\rangle\|\downarrow\rangle$
$D_{T(-1/2)}$	$\frac{1}{\sqrt{3}}[\|T_0\rangle\|\downarrow\rangle - \sqrt{2}\|T_-\rangle\|\uparrow\rangle]$

Table. 2 | Eigenstates of the Heisenberg spin trimer at $|\Delta B_z| \gg J_{LR}$

State	Spin expression
$Q_{(+3/2)}$	$\|T_+\rangle\|\uparrow\rangle$
$Q_{(-3/2)}$	$\|T_-\rangle\|\downarrow\rangle$
$D_{S(+1/2)}$	$\|S\rangle\|\uparrow\rangle$
$\tilde{D}_{0(+1/2)}$	$\|T_0\rangle\|\uparrow\rangle$
$\tilde{D}_{1(+1/2)}$	$\|T_+\rangle\|\downarrow\rangle$
$D_{S(-1/2)}$	$\|S\rangle\|\downarrow\rangle$
$\tilde{D}_{0(-1/2)}$	$\|T_0\rangle\|\downarrow\rangle$
$\tilde{D}_{1(-1/2)}$	$\|T_-\rangle\|\uparrow\rangle$

excited (e) or ground (g) state. P(A | B) refers to the conditional probability of A given B. According to the Bayes theorem, $P(f_1, f_2|\,M_n) = P(M_n\,|\,f_1, f_2)\,P(f_1, f_2)/P(M_n)$, where a uniform distribution of $P(f_1, f_2)$ over the f_1 and f_2 space is supposed for simplicity. Assuming each measurement is not affected by the previous ones, $P(f_1, f_2|M_1, M_2, \ldots, M_N) = \prod_{n=1}^{N} P(f_1, f_2|M_n) \propto \prod_{n=1}^{N} P(M_n|f_1, f_2)$ holds.

For the efficient real-time estimation of the frequencies, we utilize a field-programmable-gate-array (FPGA, Digilent Zedboard) to update the probability distribution as soon as each measurement result is sent to the FPGA. After 300 measurements, the FPGA outputs a single set of (f_1^*, f_2^*) which maximizes $P(f_1, f_2|M_1, M_2, \ldots, M_N)$. Thereby, a single estimation of the set takes ~6 ms and allows both the $D_{S(+1/2)}-\tilde{D}_{1(+1/2)}$ and $D_{S(-1/2)}-\tilde{D}_{0(-1/2)}$ fluctuations to be tracked simultaneously.

Data availability

Datasets generated during the current study are available from the corresponding author on reasonable request.

Received: 13 May 2025; Accepted: 23 November 2025;
Published online: 18 December 2025

References

1. Yang, S., Wang, X. & Das Sarma, S. Generic Hubbard model description of semiconductor quantum-dot spin qubits. *Phys. Rev. B* **83**, 161301 (2011).
2. Byrnes, T., Kim, N. Y., Kusudo, K. & Yamamoto, Y. Quantum simulation of Fermi-Hubbard models in semiconductor quantum-dot arrays. *Phys. Rev. B* **78**, 075320 (2008).
3. Imada, M., Fujimori, A. & Tokura, Y. Metal-insulator transitions. *Rev. Mod. Phys.* **70**, 1039–1263 (1998).
4. Petta, J. R. et al. Coherent manipulation of coupled electron spins in semiconductor quantum dots. *Science* **309**, 2180–2184 (2005).
5. Loss, D. & DiVincenzo, D. P. Quantum computation with quantum dots. *Phys. Rev. A* **57**, 120–126 (1998).
6. Dehollain, J. P. et al. Nagaoka ferromagnetism observed in a quantum dot plaquette. *Nature* **579**, 528–533 (2020).
7. Van Diepen, C. J. et al. Quantum simulation of antiferromagnetic Heisenberg chain with gate-defined quantum dots. *Phys. Rev. X* **11**, 041025 (2021).
8. Hensgens, T. et al. Quantum simulation of a Fermi–Hubbard model using a semiconductor quantum dot array. *Nature* **548**, 70–73 (2017).
9. Shi, Z. et al. Fast hybrid silicon double-quantum-dot qubit. *Phys. Rev. Lett.* **108**, 140503 (2012).
10. DiVincenzo, D. P., Bacon, D., Kempe, J., Burkard, G. & Whaley, K. B. Universal quantum computation with the exchange interaction. *Nature* **408**, 339–342 (2000).
11. Lidar, D. A., Chuang, I. L. & Whaley, K. B. Decoherence-free subspaces for quantum computation. *Phys. Rev. Lett.* **81**, 2594–2597 (1998).
12. Kielpinski, D. et al. A decoherence-free quantum memory using trapped ions. *Science* **291**, 1013–1015 (2001).
13. Danon, J., Chatterjee, A., Gyenis, A. & Kuemmeth, F. Protected solid-state qubits. *Appl. Phys. Lett.* **119**, 260502 (2021).
14. Friesen, M., Ghosh, J., Eriksson, M. A. & Coppersmith, S. N. A decoherence-free subspace in a charge quadrupole qubit. *Nat. Commun.* **8**, 15923 (2017).
15. Levy, J. Universal quantum computation with spin- 1 / 2 pairs and heisenberg exchange. *Phys. Rev. Lett.* **89**, 147902 (2002).
16. Sala, A., Qvist, J. H. & Danon, J. Highly tunable exchange-only singlet-only qubit in a GaAs triple quantum dot. *Phys. Rev. Res.* **2**, 012062 (2020).
17. Sala, A. & Danon, J. Exchange-only singlet-only spin qubit. *Phys. Rev. B* **95**, 241303 (2017).
18. Yannouleas, C. & Landman, U. Symmetry breaking and quantum correlations in finite systems: studies of quantum dots and ultracold Bose gases and related nuclear and chemical methods. *Rep. Prog. Phys.* **70**, 2067 (2007).
19. Yannouleas, C. & Landman, U. Wigner molecules and hybrid qubits. *J. Phys. Condens. Matter* **34**, 21LT01 (2022).
20. Wigner, E. On the interaction of electrons in metals. *Phys. Rev.* **46**, 1002–1011 (1934).
21. Yannouleas, C. & Landman, U. Molecular formations and spectra due to electron correlations in three-electron hybrid double-well qubits. *Phys. Rev. B* **105**, 205302 (2022).
22. Abadillo-Uriel, J. C., Martinez, B., Filippone, M. & Niquet, Y.-M. Two-body Wigner molecularization in asymmetric quantum dot spin qubits. *Phys. Rev. B* **104**, 195305 (2021).
23. Jang, W. et al. Single-shot readout of a driven hybrid qubit in a GaAs double quantum dot. *Nano Lett.* **21**, 4999–5005 (2021).
24. Jang, W. et al. Wigner-molecularization-enabled dynamic nuclear polarization. *Nat. Commun.* **14**, 2948 (2023).
25. Shapir, I. et al. Imaging the electronic Wigner crystal in one dimension. *Science* **364**, 870–875 (2019).
26. Pecker, S. et al. Observation and spectroscopy of a two-electron Wigner molecule in an ultraclean carbon nanotube. *Nat. Phys.* **9**, 576–581 (2013).
27. Corrigan, J. et al. Coherent control and spectroscopy of a semiconductor quantum dot wigner molecule. *Phys. Rev. Lett.* **127**, 127701 (2021).
28. De Palma, F. et al. Strong hole-photon coupling in planar Ge for probing charge degree and strongly correlated states. *Nat. Commun.* **15**, 10177 (2024).
29. Shulman, M. D. et al. Suppressing qubit dephasing using real-time Hamiltonian estimation. *Nat. Commun.* **5**, 5156 (2014).
30. Nakajima, T. et al. Coherence of a driven electron spin qubit actively decoupled from quasistatic noise. *Phys. Rev. X* **10**, 011060 (2020).

31. Kim, J. et al. Approaching ideal visibility in singlet-triplet qubit operations using energy-selective tunneling-Based Hamiltonian estimation. *Phys. Rev. Lett.* **129**, 040501 (2022).
32. Kim, D. et al. Quantum control and process tomography of a semiconductor quantum dot hybrid qubit. *Nature* **511**, 70–74 (2014).
33. Hanson, R., Kouwenhoven, L. P., Petta, J. R., Tarucha, S. & Vandersypen, L. M. K. Spins in few-electron quantum dots. *Rev. Mod. Phys.* **79**, 1217–1265 (2007).
34. Reilly, D. J., Marcus, C. M., Hanson, M. P. & Gossard, A. C. Fast single-charge sensing with a rf quantum point contact. *Appl. Phys. Lett.* **91**, 162101 (2007).
35. Wang, Z. et al. Jellybean quantum dots in silicon for qubit coupling and on-chip quantum chemistry. *Adv. Mater.* **35**, 2208557 (2023).
36. Elzerman, J. M., Hanson, R., Willems van Beveren, L. H., Vandersypen, L. M. K. & Kouwenhoven, L. P. Excited-state spectroscopy on a nearly closed quantum dot via charge detection. *Appl. Phys. Lett.* **84**, 4617–4619 (2004).
37. Elzerman, J. M. et al. Single-shot read-out of an individual electron spin in a quantum dot. *Nature* **430**, 431–435 (2004).
38. Jang, W. et al. Robust energy-selective tunneling readout of singlet-triplet qubits under large magnetic field gradient. *npj Quantum Inf.* **6**, 1–7 (2020).
39. Kim, D. et al. Microwave-driven coherent operation of a semiconductor quantum dot charge qubit. *Nat. Nanotechnol.* **10**, 243–247 (2015).
40. Shi, Z. et al. Fast coherent manipulation of three-electron states in a double quantum dot. *Nat. Commun.* **5**, 3020 (2014).
41. Petta, J. R. et al. Dynamic nuclear polarization with single electron spins. *Phys. Rev. Lett.* **100**, 067601 (2008).
42. Foletti, S., Bluhm, H., Mahalu, D., Umansky, V. & Yacoby, A. Universal quantum control of two-electron spin quantum bits using dynamic nuclear polarization. *Nat. Phys.* **5**, 903–908 (2009).
43. Hanson, R. et al. Zeeman energy and spin relaxation in a one-electron quantum Dot. *Phys. Rev. Lett.* **91**, 196802 (2003).
44. Redfield, A. G. Spatial diffusion of spin energy. *Phys. Rev.* **116**, 315–316 (1959).
45. A Coherent Beam Splitter for Electronic Spin States. https://www.science.org/doi/10.1126/science.1183628 10.1126/science.1183628.
46. Delbecq, M. R. et al. Quantum dephasing in a gated GaAs triple quantum dot due to nonergodic noise. *Phys. Rev. Lett.* **116**, 046802 (2016).
47. Metzler, R. & Klafter, J. The random walk's guide to anomalous diffusion: a fractional dynamics approach. *Phys. Rep.* **339**, 1–77 (2000).
48. Philips, S. G. J. et al. Universal control of a six-qubit quantum processor in silicon. *Nature* **609**, 919–924 (2022).
49. Song, Y. et al. Coherence of a field gradient driven singlet-triplet qubit coupled to multielectron spin states in 28Si/SiGe. *npj Quantum Inf.* **10**, 77 (2024).
50. Jirovec, D. et al. A singlet-triplet hole spin qubit in planar Ge. *Nat. Mater.* **20**, 1106–1112 (2021).

Acknowledgements

This work was supported by a National Research Foundation of Korea (NRF) grant funded by the Korean Government (MSIT) (No. 2019M3E4A1080144, No. 2019M3E4A1080145, No. 2019R1A5A1027055, No. RS-2023-00283291, SRC Center for Quantum Coherence in Condensed Matter No. RS-2023-00207732, No. RS-2024-00442994, No. RS-2024-00413957, and No. 2023R1A2C2005809), a Korea Basic Science Institute (National Research Facilities and Equipment Center) grant funded by the Ministry of Education (No. 2021R1A6C101B418). Correspondence and requests for materials should be addressed to D.K. (dohunkim@snu.ac.kr).

Author contributions

D.K. and W.J. conceived the project. W.J. performed the measurements with J.K. W.J. analyzed the data. J.K. and H. Jung fabricated the device. J.P., M.C., H. Jang, and S.S. built the experimental setup and configured the measurement software. V.U. synthesized and provided the GaAs heterostructure. All the authors contributed to the preparation of the manuscript.

Competing interests

The authors declare no competing interests.

Additional information

Supplementary information The online version contains supplementary material available at https://doi.org/10.1038/s41534-025-01151-5.

Correspondence and requests for materials should be addressed to Dohun Kim.